Batteries & Supercaps

Research Article
doi.org/10.1002/batt.202300430

Chemistry
Europe
European Chemical
Societies Publishing

www.batteries-supercaps.org

Hydrothermal Synthesis of a Graphene-based Composite Enabling the Fabrication of a Current Collector-free Microsupercapacitor with Improved Energy Storage Performance

Adnane Bouzina,[a] René Meng,[a] Françoise Pillier,[a] Hubert Perrot,[a] Ozlem Sel,*[b, c] and Catherine Debiemme-Chouvy*[a]

Herein, the development and the characterization of an all-solid-state symmetrical and current collector-free microsupercapacitor based on a new reduced graphene oxide-polydopamine (rGO-PDA) composite are reported. The rGO-PDA composite is synthesized by a facile, eco-friendly and scalable hydrothermal approach in the presence of dopamine which can not only contribute to the oxygen functional groups removal from graphene oxide but also polymerize onto the rGO sheets reducing their restacking and improving the wettability of the electrode. The optimized rGO-PDA composite material exhibits excellent capacitance and cycling stability as well as an improved rate capability compared to the pristine rGO in Na_2SO_4 solution. This performance enhancement can be linked to the higher transfer kinetic and lower transfer resistance values of the ions involved in the charge storage process of rGO-PDA, as determined by *ac*-electrogravimetry. Furthermore, an all-solid-state microsupercapacitor was prepared employing the optimized rGO-PDA composite as electrode material. Interdigitated electrodes were obtained thanks to a CO_2 laser and a Na_2SO_4/PVA hydrogel was employed, no current collector was used. This device achieves a noteworthy energy density of 6.2 mWh·cm^{-3} at a power density of 0.22 W·cm^{-3}. Moreover, it exhibits exceptional cycling stability, retaining 104% of its initial capacity even after undergoing 10,000 cycles at 2 V·s^{-1}.

Introduction

Micro-scale energy storage devices have become notably essential in the development of portable and wearable electronic devices.[1–5] Among the various micro-scale energy storage devices, micro-supercapacitors and micro-batteries have gained significant attention owing to their unique properties and potential applications. While micro-batteries have been the traditional choice for energy storage in microelectronics, microsupercapacitors have emerged as a promising alternative due to their higher power density, faster charge and discharge rates, and longer cycle life.[6–8] For instance, microsupercapacitors have been shown to possess significant promise in powering wearable electronics, such as smartwatches and fitness trackers, due to their high-power density and fast charging capabilities.[9,10]

Graphene, a two-dimensional material, has emerged as a promising material for microsupercapacitors. Owing to its high surface area, excellent electrical conductivity, and mechanical strength, graphene-based microsupercapacitors offer several advantages including high power density, long cycle life, and the potential for easy integration into microelectronic devices. As a result, graphene-based microsupercapacitors have attracted significant research interest and hold great promise for a wide range of applications.[11–13]

For the synthesis of graphene, several methods have been developed comprising chemical vapor deposition, liquid-phase exfoliation, and reduction of graphene oxide (GO).[14–17] Among these methods, the hydrothermal reduction of GO has emerged as a promising approach for the synthesis of graphene due to its advantages over other methods. Hydrothermal reduction of GO offers several advantages, such as low cost, ease of production, scalability, and the potential for tailoring the properties of the resulting graphene.[18,19] In recent years, there has been growing interest in using green reducing agents to replace toxic and harmful reducing agents in the hydrothermal reduction process. Among the reductors, dopamine (DA), a natural catecholamine neurotransmitter, has shown great potential as a green reducing agent for reducing GO. It has been demonstrated that in a solution synthesis involving the dopamine and GO, dopamine can not only remove oxygen functional groups from graphene oxide but also self-polymerize on the rGO sheets which reduces the restacking of the

[a] Dr. A. Bouzina, R. Meng, F. Pillier, Dr. H. Perrot, Dr. C. Debiemme-Chouvy
Sorbonne Université, CNRS, Laboratoire Interfaces et Systèmes Electro-chimiques, LISE UMR 8235, 4 place Jussieu, F-75005 Paris, France
E-mail: catherine.debiemme-chouvy@sorbonne-universite.fr

[b] Dr. O. Sel
Chimie du Solide et de l'Energie, UMR 8260, Collège de France, 11 Place Marcelin Berthelot, F-75231 Paris Cedex 05, France
E-mail: ozlem.sel@college-de-france.fr

[c] Dr. O. Sel
Réseau sur le Stockage Electrochimique de l'Energie (RS2E), CNRS FR 3459, 33 Rue Saint Leu, F-80039 Amiens Cedex, France

graphene sheets and improves the wettability of the electrode due to the presence of the nitrogen in PDA.[20–24]

Here, we present a cost-effective and environmentally friendly approach for large-scale production of reduced graphene oxide (rGO) using the hydrothermal method, leveraging the multifunctional properties of polydopamine (PDA). The optimized composite material, rGO-PDA, exhibits improved volumetric and gravimetric capacitances, superior cycling stability and enhanced transfer kinetics as well as low transfer resistance for the species involved in the charge balance process compared to pristine rGO. Finally, a current collector free solid-state interdigitated microsupercapacitor was successfully fabricated using the optimized composite through laser cutting and tests with a gel electrolyte interface presented remarkable charge storage performance.

Results and Discussion

Optimization of the rGO-PDA composite

After the hydrothermal treatment of the GO suspension containing dopamine, a black powder was obtained by vacuum filtration (Figure S1). Various rGO-PDA composites were prepared (see Experimental Section). In order to obtain an rGO-PDA composite material with optimized capacitance, the influence of the initial DA/GO ratio (Table S1) on the electrochemical response of the final product was investigated. Figure S2 shows the voltammograms of the various materials tested (DA/GO mass ratio: 0.5 to 4). A quasi-rectangular signal is observed for all these electrodes (Figure S2 and 1A). From these voltammograms, the gravimetric capacitances (C_g in $F \cdot g^{-1}$) at two scan rates (10 and 100 $mV \cdot s^{-1}$) were calculated, they are shown in Figure 1B. From this figure, it is clear that the rGO-PDA composite obtained with an initial DA/GO ratio of 2 has the highest gravimetric capacitance (208 $F \cdot g^{-1}$ at 10 $mV \cdot s^{-1}$) and is therefore considered to be the optimized composite. Its electrochemical response is shown in Figure 1A.

Morphological and compositional analyses of rGO-PDA composite

Figure 2A shows the XRD patterns of the three samples GO, rGO and optimized rGO-PDA deposited on a glass substrate. The pattern of GO shows the (001) diffraction peak at $2\theta = 10.5°$ (corresponding to a d-spacing of 0.842 nm), which is in good agreement with the literature values.[25,26] After hydrothermal treatment, this characteristic peak is no longer detected. This result shows that for both samples, rGO and rGO-PDA, the graphene oxide has been successfully reduced by the hydrothermal method. For both samples a new broad peak appears around $2\theta = 23°$.

The chemical composition of GO, rGO, and rGO-PDA films deposited on gold-coated mica was determined by XPS. Figure 2B shows the XPS survey spectra obtained for these samples and Table S2 shows the chemical composition in atomic % of their surface. For the optimal rGO-PDA composite (DA/GO = 2), PDA nitrogen is detected around a binding energy of 400 eV (Figure 2B). The atomic N/C ratio for the rGO-PDA composite is 0.053 whereas it is 0.123 for the PDA (theoretical value: 0.125 based on the DA formula $C_8H_{11}NO_2$) (Table S2).[27] The low N/C ratio confirms that this material is a composite of rGO and PDA.

In order to determine the density of rGO and rGO-PDA, films were first formed by drop casting on a quartz electrode to determine their mass. Thanks to nanogram sensitivity of QCM, the mass loading of the electrodes was estimated to be 7.8 μg for rGO and 8.5 μg for rGO-PDA film. The thickness of rGO and rGO-PDA films were then estimated from the SEM observations (Figure 2C and 2D) allowing us to calculate their volume (the geometric area of the two films being 0.2 cm^2). The density of the rGO-PDA composite was estimated to be 1.69 $g \cdot cm^{-3}$ and those of the rGO to be 1.55 $g \cdot cm^{-3}$. The slight difference in densities observed between the two films could be explained by the presence of PDA between the rGO sheets.

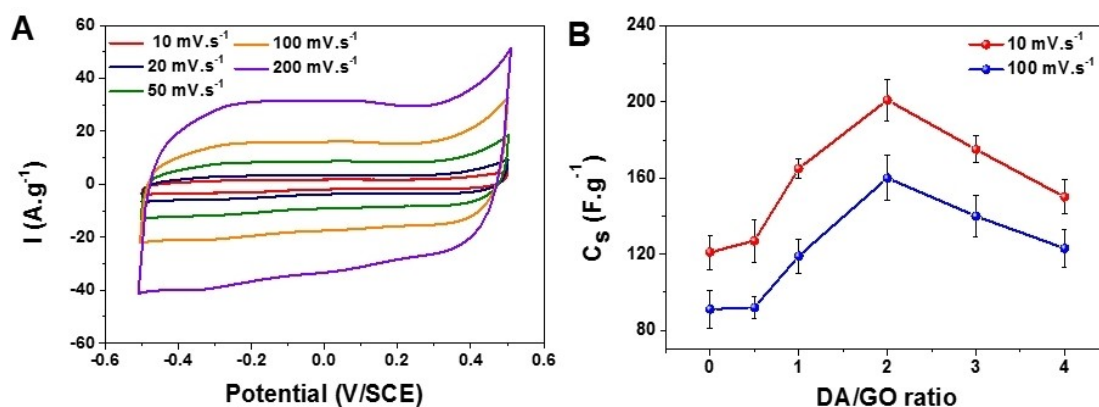**Figure 1.** (A) Cyclic voltammograms of the optimized rGO-PDA prepared with a DA/GO ratio of 2, in 0.5 M Na_2SO_4 at different scan rates. (B) Gravimetric capacitance at two scan rates (10 and 100 $mV \cdot s^{-1}$) of the rGO-PDA composite film obtained with different DA/GO mass ratios.

Batteries & Supercaps

Research Article
doi.org/10.1002/batt.202300430

Chemistry Europe
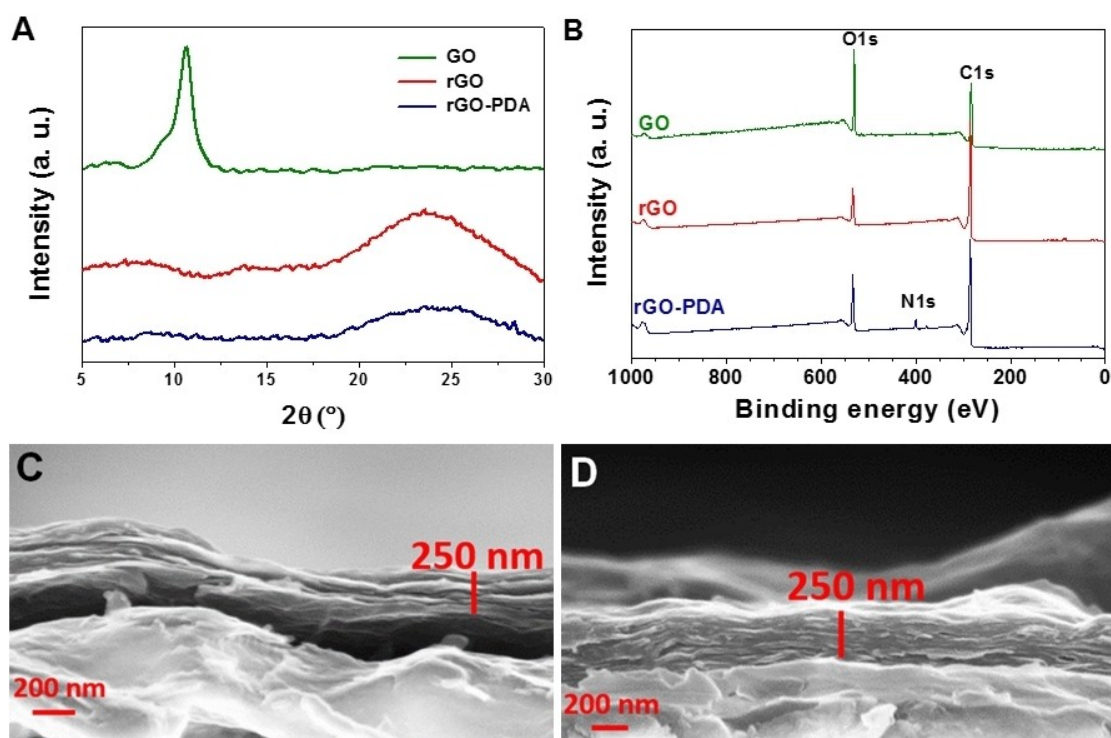European Chemical
Societies Publishing

Figure 2. (A) Diffractograms of GO, rGO and optimized rGO-PDA films (DA/GO mass ratio = 2). (B) XPS survey spectra from GO, rGO, and optimized rGO-PDA films. SEM micrographs of the cross-section of (C) rGO and (D) rGO-PDA films on Au/quartz.

Electrogravimetric behavior of rGO and rGO-PDA in 0.5 M Na_2SO_4

Figure 3 shows the current-mass voltammograms of rGO and rGO-PDA films, as a function of potential, obtained at different scan rates from 10 to 2000 mV·s^{-1} for cyclic voltammetry and from 10 to 200 mV·s^{-1} for mass/potential curves.

Figure S3, 4A and 4B show the galvanostatic charge-discharge curves for these two films at different current densities and the associated mass changes. It is clearly seen that for both films, the mass decreases during charging (Figure S3B and 4B) (or anodic sweep of potential for potentiodynamic cycling) (Figure 3C and 3D) and increases during discharging (Figure S3A and 4B) (or cathodic sweep of potential for potentiodynamic cycling (Figure 3C and 4D)). These results indicate that the electroneutrality of rGO and rGO-PDA is mainly maintained by the participation of cations.

Since both rGO and rGO-PDA electrodes have almost the same mass loading, the high discharge times (151 s for rGO-PDA *versus* only 80 s for rGO at a current density of 0.1 mA·cm^{-2}) observed during charge-discharge cycles for the rGO-PDA composite compared to the rGO (Figure 4A and S3A) may indicate a larger surface area developed for the charge storage process for the composite electrode. In addition, the absence of hysteresis in the mass response of the rGO-PDA composite electrode in contrast to the rGO (Figure 4B and S3B) indicates that electroadsorption and electrodesorption of the species involved in the charge compensation process occur at very similar rates.

From the EQCM measurements, an interesting function, the mass per electron (MPE), Fdm/dq, can be calculated. This value allows to estimate the average molar mass of the ions involved in the charge compensation process within the electrode. If solely one species is involved, the MPE corresponds to its molar mass. The Fdm/dq function of the rGO-PDA composite upon charging and discharging for three current densities (0.25, 0.5, and 2 mA.cm^{-2}) was calculated (from the QCM-GCD response (Figure 4A and 4B)). Figure 4C and 4D show the calculated MPE values as a function of the imposed potential. For the three current densities, the Fdm/dq curves have a similar shape. The variation of the MPE with potential and its deviation from 23 g.mol^{-1} (corresponding to a bare Na$^+$) can be explained by the participation of more than one species in the charge compensation process. Ac-electrogravimetry remains the only gravimetric technique that can identify the number and nature of species participating directly or indirectly in the charge compensation process.

Ac-electrogravimetry

In order to find out the species involved in the charge compensation process and to have information on their transfer kinetics at the electrolyte/electrode interface, ac-electrogravimetry measurements were performed at several potentials over the range of −0.5 to 0.5 V/SCE. Figure 5A shows the charge/potential transfer function, $\Delta q/\Delta E(\omega)$, of rGO and rGO-PDA at a potential of −0.3 V/SCE. This transfer function can reveal the
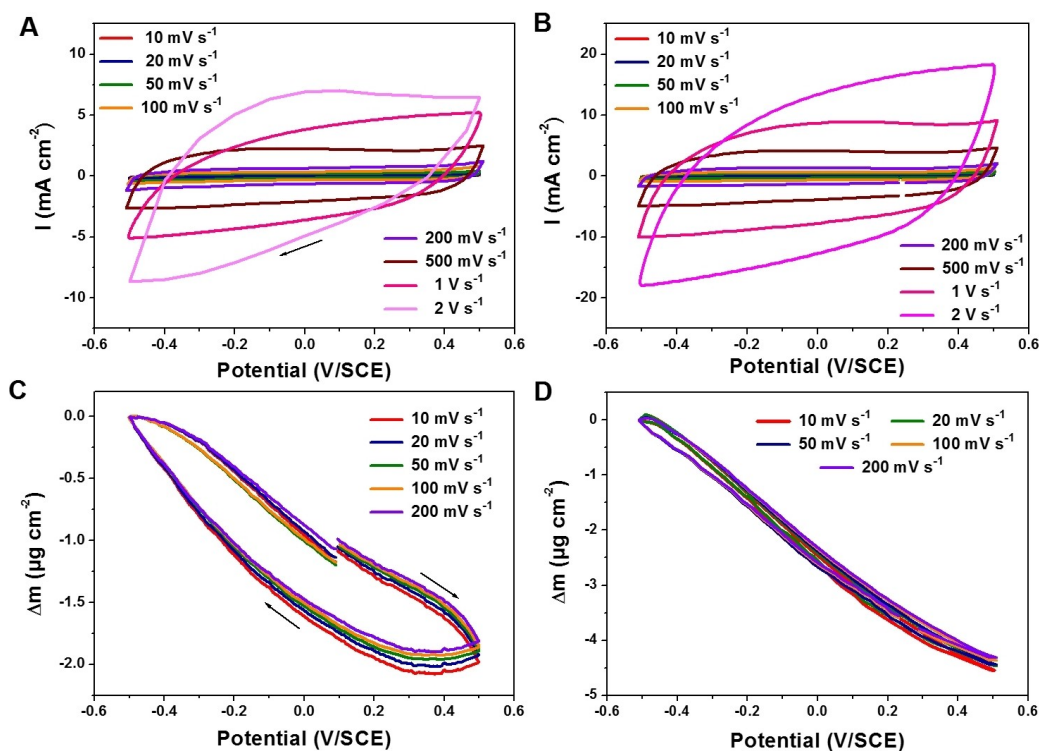
Figure 3. Voltammograms for (A) rGO and (B) rGO-PDA and mass variation *versus* potential for (C) rGO and (D) rGO-PDA at various potential scan rates, in 0.5 M Na_2SO_4 solution.
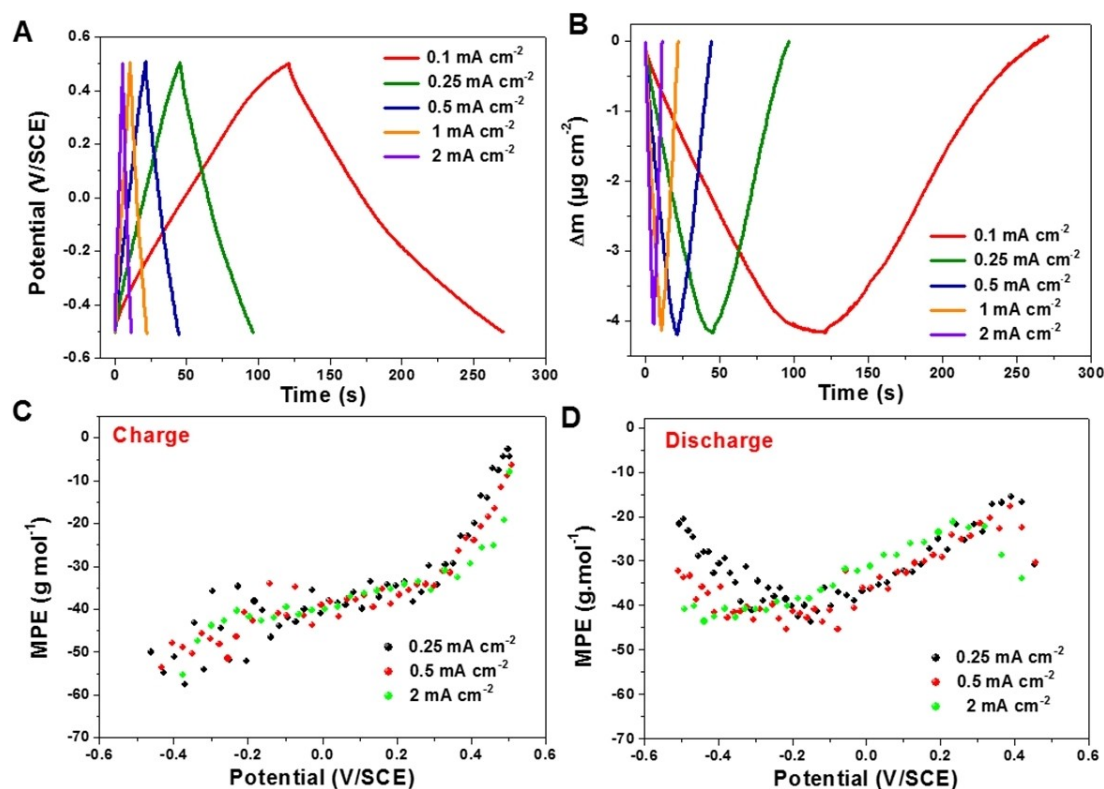

Figure 4. (A) Potential variation with time and (B) mass variation with time, related to galvanostatic charge/discharge of the optimized rGO-PDA at different current densities in 0.5 M Na_2SO_4. MPE function calculated from the QCM-CDG response at different current densities during (C) charge and (D) discharge for the rGO-PDA composite.
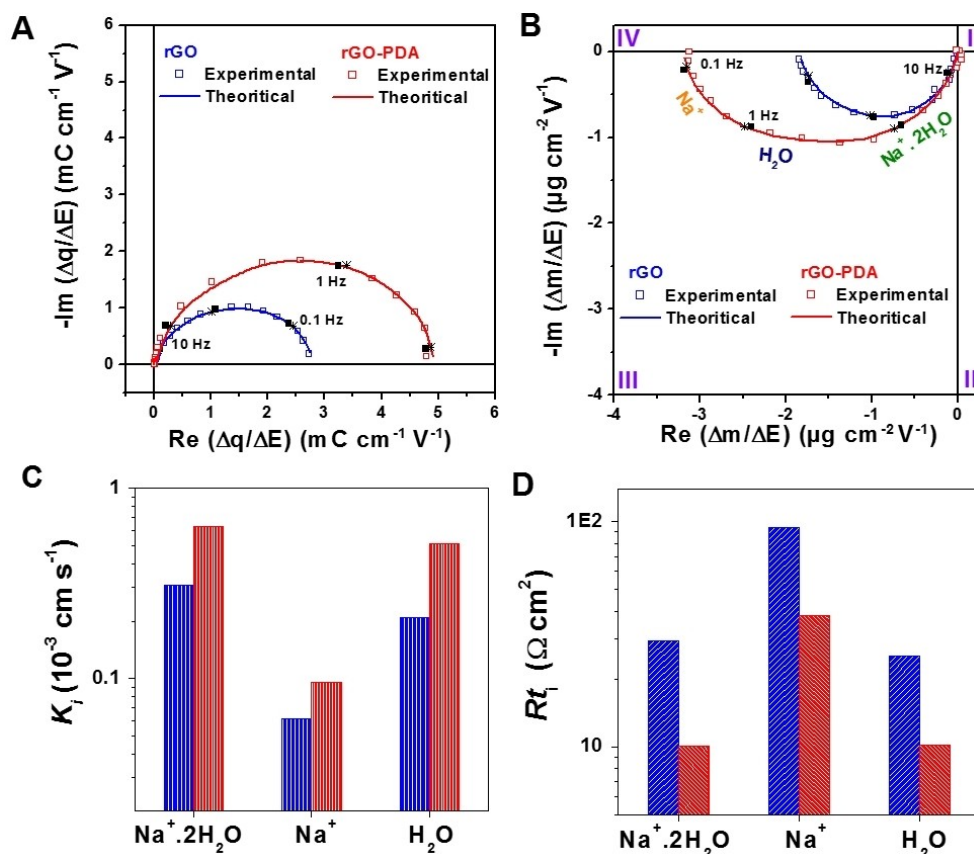
Batteries & Supercaps

Research Article
doi.org/10.1002/batt.202300430

Chemistry
Europe
European Chemical
Societies Publishing

Figure 5. Experimental and theoretical transfer functions of rGO (blue) and rGO-PDA (red) electrodes at a potential of -0.3 V *vs.* SCE: (A) $\Delta q/\Delta E(\omega)$ and (B) $\Delta m/\Delta E(\omega)$, in 0.5 M Na_2SO_4 solution. (C) K_i and (D) Rt_i of ions and water molecule at -0.3 V *vs.* SCE for rGO (blue) and rGO-PDA (red).

contribution of charged species involved in the charge compensation process. The charge/potential transfer function curves, $\Delta q/\Delta E(\omega)$, of the two electrodes (Figure 5A) show a depressed loop, which can be attributed to the participation of more than one charged species with fairly close ion transfer constants at the interface. It is important to note that the $\Delta q/\Delta(\omega)$ loop diameter is larger for rGO-PDA, indicating that more ions are involved in the charge compensation of the composite electrode (knowing that both films have similar mass). This result is very consistent with the current densities achieved by cyclic voltammetry between these two electrodes (Figure 3).

The experimental charge/potential transfer function data, $\Delta q/\Delta(\omega)$, were fitted with the theoretical function given by Equation S2. Good agreement was obtained between the theoretical and experimental curves by taking into account the involvement of two ionic species. Two parameters, related to kinetics of interfacial transfer and inverse of the transfer resistance (K_i and) for each of these two species were obtained by this fitting process, and are reported in Table S3.

The $\Delta q/\Delta E(\omega)$ transfer function provides information on the contribution of charged species but does not allow for their identification. For this, simultaneously measured electrogravimetric transfer function, $\Delta m/\Delta(\omega)$, was analyzed to identify both charged and neutral (solvent) species. For both films (rGO and rGO-PDA), the electrogravimetric responses, $\Delta m/\Delta(\omega)$, are in the third quadrant, consistent with the transfer of cationic species

or cationic species with solvent (Figure 5B). The two parameters, K_i and G_i, for the two ionic species previously obtained from Equation S2 (Table S3) were used for fitting the electrogravimetric transfer function, $\Delta m/\Delta(\omega)$, (Equation S3). The additional parameters, K_i and G_i for the free solvent molecules as well as the molar mass (M_i) of each species were estimated after fitting.

The process of fitting the experimental $\Delta m/\Delta(\omega)$ curves reveals the participation of two cations: $Na^+ \cdot 2H_2O$ at high frequencies and Na^+ at low frequencies. Free H_2O molecules were detected at intermediate frequencies. The transfer order of the two cations as well as the participation of free water is consistent with *ac*-electrogravimetry measurements previously performed on carbon materials in similar electrolytes.[28–31]

The interfacial transfer constants, K_i, of the different species involved in the charge compensation process as a function of the applied potential for rGO and rGO-PDA are shown in Figure S4. From this figure, it is clear that the three exchanged species transfer faster at the composite electrode interface, rGO-PDA, compared to that at the rGO. As an example, the interfacial transfer kinetics of $Na^+ \cdot 2H_2O$ cation is twice faster at the rGO-PDA interface compared to rGO (Figure 5C). This finding underlines faster charge-discharge kinetics for the rGO-PDA composite. In addition, this composite shows lower transfer resistance, Rt_i, compared to the rGO electrode whatever the species (Figure 5D).

Correlation between EQCM and ac-electrogravimetry results

To validate our assumption concerning the involvement of three species in the charge storage process in rGO and rGO-PDA, we used a methodology that takes advantage of the complementarity between EQCM and *ac*-electrogravimetry.[28,32]

Using the parameters K_i (Figure S4) and G_i obtained by fitting the experimental transfer functions, the relative concentration variation, $C_i - C_0$, of the species, identified by exploitation of the *ac*-electrogravimetry data, as a function of the applied potential can be estimated. This quantity is calculated by the low-frequency integration of Equation S4 and shown in Equation 5. Figure S5A and S5B show the variations of the relative concentration, $C_i - C_0$, of the three species identified for rGO and rGO-PDA films ($Na^+ \cdot 2H_2O$, H_2O and Na^+) as a function of the potential. For both films, the free solvent (H_2O) shows the largest concentration variation in the potential range of −0.5 to 0.5 V/SCE.

From the relative concentration variations (Figure S5A and S5B), the mass variations of each species (Δm_i) as a function of the potential can be calculated by considering the molar mass of each (Figure S5C and S5D). Reconstruction of the global mass change can be performed by adding the contributions of the individual mass changes (Figure S6). A good agreement is obtained between the mass measured with conventional EQCM at 10 mV·s^{-1} and the mass reconstructed from *ac*-electrogravimetry in the potential range studied for both rGO and rGO-PDA films. This result confirms the participation of the three species in the charge storage process ie. $Na^+ \cdot H_2O$, Na^+ and H_2O.

Evaluation of the charge storage performance of the rGO-PDA composite

The capacitances were calculated from the cyclic voltammograms depicted in Figure 3. Figure 6A and 6B show the gravimetric and volumetric capacitances as a function of scan rate, for rGO and rGO-PDA, respectively. From these figures it is obvious that the rGO-PDA composite has higher gravimetric capacitances and voltammetric capacitances than the rGO. At a scan rate of 10 mV·s^{-1}, rGO-PDA has a volume capacitance of 351 F·cm^{-3} and a gravimetric capacitance of 208 F·g^{-1} compared to only 185 F·cm^{-3} and 121 F·g^{-1} for rGO which is higher than those reported for carbon-based electrodes for EDLCs.[33–36]

The rGO-PDA composite also exhibits better capacitance retention as the scan rate increases. Indeed, rGO-PDA has a capacitance of 208 F·g^{-1} at 10 mV·s^{-1} and 95 F·g^{-1} at 2000 mV·s^{-1} (i.e., 45% retention) while rGO has a capacitance of 121 F·g^{-1} at 10 mV·s^{-1} and 30 F·g^{-1} at 2000 mV·s^{-1}, corresponding to 45% and 25% capacitance retention, respectively. These results which indicate faster charge/discharge kinetics for the composite electrode are in good agreement with the lower time constant of rGO-PDA compared to the pristine rGO (Figure S7 and Table S4).

The cycling stability of both rGO and rGO-PDA films was studied by cyclic voltammetry at a scan rate of 2 V·s^{-1} (Figure 6C and 6D). The composite electrode shows excellent cycling stability. Indeed, the rGO-PDA whose initial capacitance is 155 F·g^{-1}, stabilizes at 152 F·g^{-1} after 10,000 cycles, i.e. a decrease of 1.5% and thus a capacitance retention of 98.5% against only 94% for the rGO.
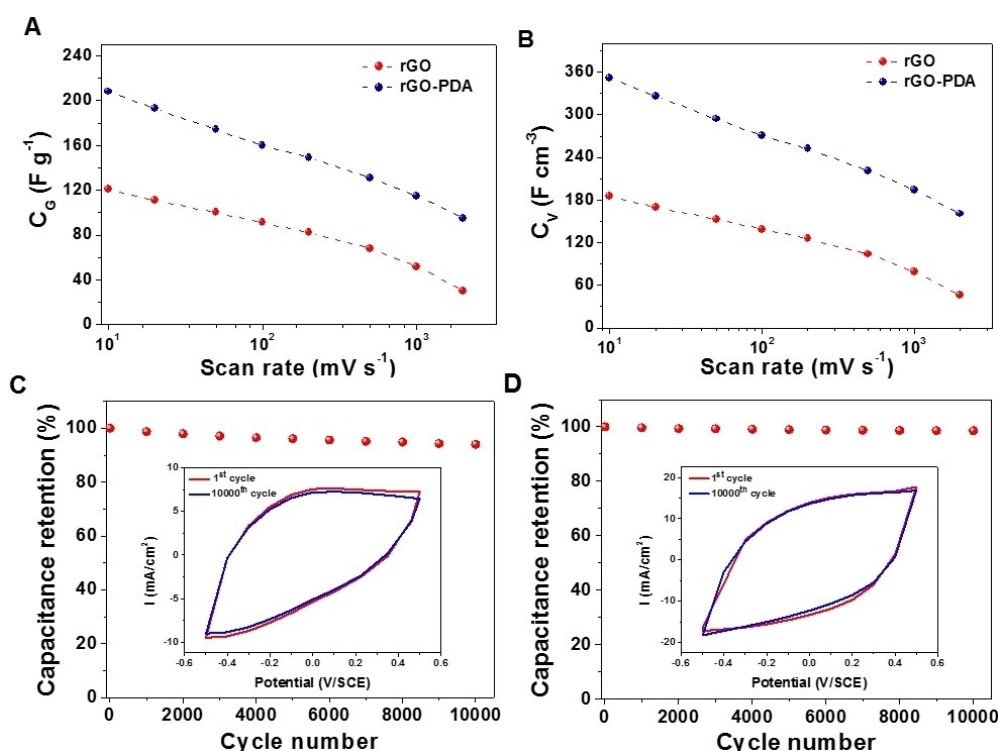

Figure 6. Variation of (A) gravimetric and (B) volumetric capacitance of rGO and rGO-PDA as a function of the potential scan rate. Cycling stability of (C) rGO and (D) rGO-PDA at a scan rate of 2 V·s^{-1} in 0.5 M Na_2SO_4.

Microsupercapacitor based on rGO-PDA composite electrodes

Figure 7A depicts a digital image of the rGO-PDA MSC fabricated on a Plexiglas substrate. This MSC is composed of 12 (2×6) interdigital fingers. Each interdigital finger has a width of around 500 μm. The global surface area covered by the interdigital electrodes is 75 mm². The inter-electrode interdigital spacing has been set at 200 μm. It's worth mentioning that no residual material resulting from the etching is observed within the interfinger space, guaranteeing the absence of short circuits in the microdevice (an ohmmeter was also used for verification purposes). A SEM image of the cross-section of an interdigital finger composed of rGO-PDA is presented in Figure 7B. It can be clearly seen that the rGO-PDA film deposited on the Plexiglass substrate is 600 nm thick. The electrochemical behavior of the rGO-PDA MSC, without current collector, was first evaluated by cyclic voltammetry and galvanostatic charge-discharge using a gel electrolyte (Na₂SO₄/PVA) (Figure 7C and 7D). The voltammograms of this MSC at different scan rates are plotted in Figure 7C and 7D. It can be clearly noticed a deviation from the voltammograms obtained in the three-electrode configuration (Figure 3B). This can be attributed to an increase in the resistance of the micro-device due to the absence of a current collector and the gel electrolyte.

Figure 7E shows the GCD curves of rGO-PDA based MSC. A triangular shape, characteristic of supercapacitors, is observed for all the tested current densities. The volumetric capacitances and the coulombic efficiency (CE) calculated from the charge-discharge curves are shown in Figure 7F. At a current density of $0.026\ \mathrm{mA\cdot cm^{-2}}$, even without a current collector, the rGO-PDA MSC exhibits a coulombic efficiency of 98% and a volumetric capacitance of $45\ \mathrm{F\cdot cm^{-3}}$.

The complex capacitance as a function of frequency was calculated from the electrochemical impedance spectroscopy measurements performed at 0.3 V, it is plotted in Figure 8A. The evolution of the imaginary capacitance $C''(\omega)$ shows a maximum
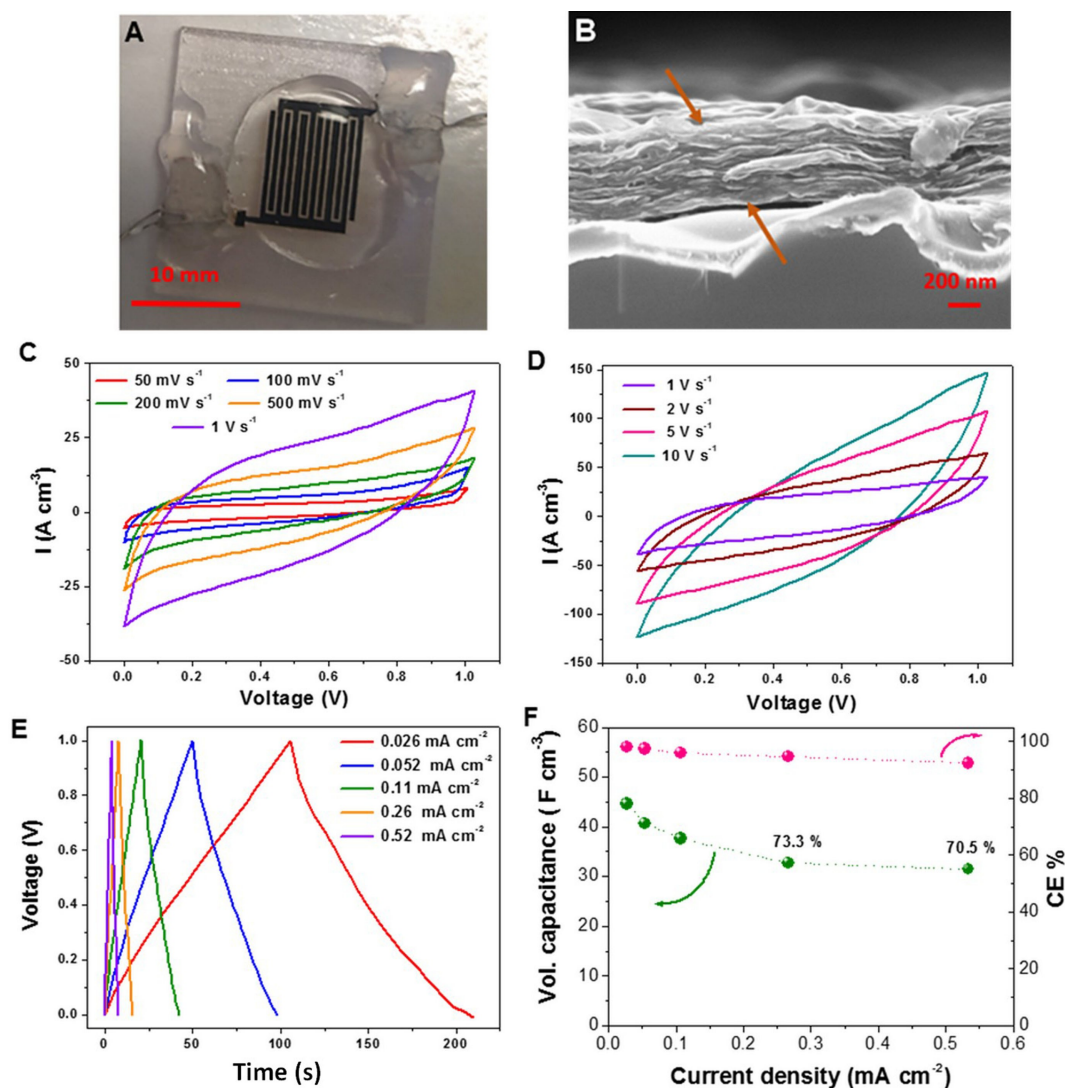

Figure 7. A) Digital photography of the rGO-PDA MSC fabricated on a Plexiglas substrate. B) SEM micrograph of the cross-section of an interdigitated rGO-PDA finger. C, D) CV curves of rGO-PDA MSC at different scan rates, from 0.05 V·s⁻¹ to 10 V·s⁻¹. E) GCD curves recorded at various current densities. F) Volumetric capacitance (left axis) and coulombic efficiency (right axis) of rGO-PDA MSC calculated from GCD curves *versus* applied current density.

Batteries & Supercaps

Research Article
doi.org/10.1002/batt.202300430

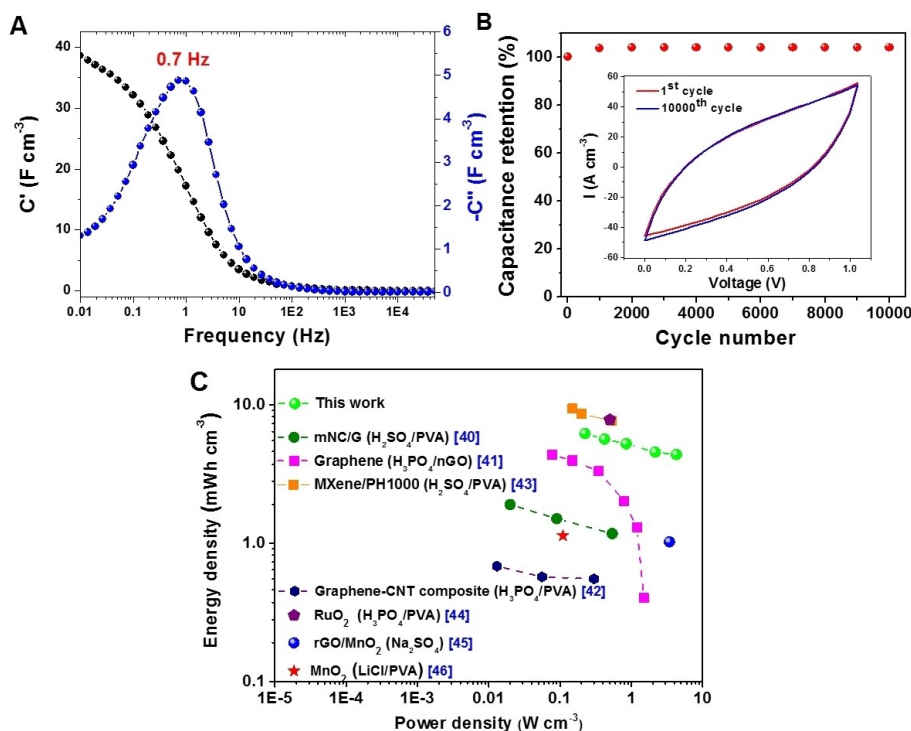**Chemistry Europe**
European Chemical
Societies Publishing

Figure 8. A) Bode plot of the volumetric capacitance of rGO-PDA MSC, determined at 0.3 V. B) Cycling stability of the rGO-PDA MSC at a scan rate of 2 V·s^{-1}. C) Ragone plot of rGO-PDA MSC (light green scatters) in comparison with some recent studies.

at a characteristic frequency (f_0) of 0.7 Hz which corresponds to a relaxation constant τ_0 of 1.43 s. The evolution of the real capacitance C′(ω) of the microdevice as a function of frequency (Figure 8A) shows a maximum capacitance of 39 F·cm^{-3} at low frequencies. This value, corresponding to the real capacitance of the microdevice, is in good agreement with the values obtained by galvanostatic charge-discharge at low current densities (Figure 7F).

The long-term cycling property of the rGO-PDA based MSC was evaluated by repeated CV cycles at a sweep rate of 2000 mV.s^{-1} within an operating voltage from 0 to 1 V. The rGO-PDA MSC exhibits a capacitance retention of 104% after undergoing 10,000 cycles (Figure 8B), the slight increase of the capacitance at the beginning of the cycling can be attributed to the activation of the composite material due to the continuous ion diffusion within the pores of the electrode material.[34,37]

Energy density and power density are crucial parameters for assessing the performance of energy storage devices. The volumetric energy and power density of the rGO-PDA MSC, calculated from the GCD profiles, are presented in the Ragone plot shown in Figure 8C. The rGO-PDA MSC demonstrates an impressive volumetric energy density of 6.20 mWh.cm^{-3} at a power density of 0.22 W.cm^{-3}. Even at a higher power density of 4.30 W.cm^{-3}, this MSC still maintains a substantial energy density of 4.33 mWh.cm^{-3}. These values exceed the performances of all-solid microsupercapacitors (with hydrogel electrolyte) reported in the literature in recent years, based on carbon materials.[38–40] Furthermore, in comparison to MSCs based on alternative material classes such as MXene[41] RuO$_2$,[42] rGO-

MnO$_x$[43] et MnO$_2$,[44] the rGO-PDA MSC developed in this work exhibits comparable energy densities.

Conclusions

In summary, an innovative and eco-friendly hydrothermal approach was developed to prepare a composite electrode based on rGO and PDA for large scale synthesis of electroactive material. The hydrothermal reduction of GO was characterized by X-ray diffraction and the presence of PDA was confirmed by XPS. The positive effect of PDA on the electrochemical performance of the rGO-PDA composite was demonstrated by the various electrogravimetric (EQCM and *ac*-electrogravimetry) and electrochemical (CV, GCD, EIS) characterization techniques. For both rGO and optimized rGO-PDA electrodes, the same species are involved in the charge compensation process. However, the kinetic constants corresponding to the interfacial transfer of the active species are greater for rGO-PDA than for rGO. This rapid charge transfer at the rGO-PDA/electrolyte interface results in fast charge/discharge kinetics (low relaxation time τ_0) and therefore better rate capability. The rGO-PDA composite material also showed good cycling stability due to the presence of the PDA between the rGO sheets, which reduces agglomeration of the rGO sheets. The results obtained for the optimized composite, in NaSO$_4$ solution and in a three-electrode configuration, motivated us to create symmetrical all-solid-state and current collector-free interdigitated micro-supercapacitors (MSCs) using a laser engraving technique, with rGO-PDA as the active material. The MSC based on rGO-PDA demonstrated

exceptional cycling stability, retaining 104% of its capacity after 10,000 cycles at $2 \, V \cdot s^{-1}$, and good rate capability without current collector. Moreover, it achieved a notable energy density of $6.20 \, mWh \cdot cm^{-3}$ at a power density of $0.22 \, W \cdot cm^{-3}$. These results outperform or are comparable to the most recently reported MSCs based on graphene or other materials.

Experimental Section

Materials

Dopamine (DA) hydrochloride, potassium phosphate monobasic (KH_2PO_4), potassium phosphate dibasic (K_2HPO_4), sodium sulfate (Na_2SO_4) and GO suspension ($4 \, mg \cdot mL^{-1}$, dispersion in H_2O) were purchased from Sigma Aldrich. The GO suspension was diluted with water to reach a concentration of $1 \, mg \cdot mL^{-1}$ of GO. All solutions were prepared with double distilled water ($18.2 \, M\Omega \cdot cm$, Purelab flex ELGA, water purification system). Phosphate buffered saline solution (PBS) with a pH of 7.2 was prepared by mixing 0.1 M of KH_2PO_4 and 0.1 M of K_2HPO_4.

Hydrothermal synthesis of rGO-PDA powder and electrode formation

In 4 mL of GO suspension (at $1 \, mg \cdot mL^{-1}$), 66.7 mg K_2HPO_4, 54.4 mg KH_2PO_4 (0.2 M PBS pH 7.2) and different amounts of dopamine (2, 4, 8, 12 and 16 mg) were solubilized. After 30 minutes in an ultrasonic bath, the suspension was transferred to a Teflon autoclave (6 mL volume) and heated to 160 °C for 8 h. For the reference rGO, the hydrothermal reaction was performed in the same way but in the absence of dopamine. After the hydrothermal treatment, a black powder was obtained by vacuum filtration, it was rinsed several times with ethanol and then bidistilled water (Figure S1). Then, the obtained powders were suspended in bidistilled water (1 mg/mL) to prepare the ink used to deposit the rGO and rGO-PDA films. The ink was homogenized by an ultrasonic probe which, unlike a conventional ultrasonic bath, allows for pulses of power to break up the aggregates more easily. In order to avoid too much heating, the agitation by the ultrasonic probe was carried out while keeping the sample (ink) in an ice bath.

For the electrogravimetric and electrochemical characterizations, 6 μL of the rGO-PDA (or rGO) suspension ($1 \, mg \cdot mL^{-1}$) were deposited on the gold electrode of the quartz resonator (AWS-Sensors, Spain) ($0.2 \, cm^2$). The rGO-PDA film was obtained after a drying step at 70 °C in an oven for 40 min. The mass of the films deposited on the quartz electrode was estimated from the frequency variation of the latter (without and with film) in air via the Sauerbrey equation.[45]

Electrochemical and electrogravimetric characterizations

The electrochemical and electrogravimetric characterizations were performed using a standard three-electrode configuration and an Autolab potentiostat (Metrohm, France). The gold electrode (0.5 cm in diameter, $0.2 \, cm^{-2}$) on a quartz (1.4 cm in diameter) (modified with rGO or rGO-PDA) was used as the working electrode, a saturated calomel electrode (SCE) and a platinum grid were used as reference electrode and counter electrode, respectively.

For the EQCM experiments, we used a lab-made QCM coupled with an Autolab potentiostat (PGSTAT12). Under the gravimetric regime, the mass variation, Δm, was obtained from Δf by using of the Sauerbrey equation ($\Delta f = -k_s \times \Delta m$), where k_s is the experimental

mass sensitivity constant which has a value of $16.3 \, Hz \cdot cm^2 \cdot g^{-1}$ for 9 MHz AT-cut QCM.[46]

The applicability of the Sauerbrey equation (verification of the gravimetric regime) on the rGO and rGO-PDA films was verified by using electroacoustic measurements.[34,47]

For *ac*-electrogravimetry measurements,[48] we employed a four-channel frequency response analyzer (FRA, Solartron 1254) and a lab-built potentiostat. The coated quartz electrode was polarized at a given potential and a sinusoidal small amplitude potential perturbation (20 mV) was applied. The frequency range of the measurements extended from 63 kHz and 10 mHz. The working electrode mass change, Δm, was measured at the same time as the *ac* response, Δl, of the electrochemical system.

Morphological and compositional characterizations

For SEM observations, a field emission gun scanning electron microscope (FEG-SEM) (Ultra55, Zeiss) operating at 5 kV was used. An Omicron Argus X-ray photoelectron spectrometer with mono-chromatized Al Kα excitation (1486.6 eV) was used for XPS analyses. For the acquisition of the survey and high-resolution spectra, the band-pass energy was fixed at 100 and 20 eV, respectively. The determination of the XPS peak area was done after subtraction of the background calculated using Shirley's method. The element peak intensities were corrected by the Scofield factors. XPS spectrum processing was performed using Casa XPS software (Casa Software Ltd., UK). For the XPS analyses, the films were deposited on a gold-coated mica substrate. XRD was recorded with a Philips PANalytical X'Pert Pro diffractometer with Cu Kα radiation ($\lambda = 1.54184 \, Å$). The films were deposited on a glass substrate.

Preparation of the rGO-PDA microsupercapacitor (MSC)

A microsupercapacitor (MSC) using the optimized rGO-PDA composite as the electrode material was produced on a Plexiglass substrate. Initially, a 2 cm square was etched on the Plexiglass substrate using a CO_2 laser cutter (Trotec SP500). Then a rGO-PDA film was deposited onto the Plexiglass substrate by drop-casting of 0.2 mL of the rGO-PDA suspension (at $1 \, mg \cdot mL^{-1}$). Finally, using the CO_2 laser, the undesired material areas (interdigitated finger spacing) were removed according to an image prepared through the Trotec JobControl® software. The laser parameters, power, scan rate and pulse duration, were set to 35 W and $35 \, cm \cdot s^{-1}$ and 1.25 ms, respectively.

Preparation of the Na_2SO_4/PVA gel electrolyte

The Na_2SO_4/PVA gel electrolyte was prepared by adding 0.25 g of Na_2SO_4 and 0.25 g of PVA into 2.5 mL of distilled water and heated to 80 °C under vigorous stirring until the solution turned transparent. Na_2SO_4/PVA gel electrolyte was subsequently drop-casted onto the interdigitated patterns and solidified overnight.

Electrochemical characterizations of the all-solid-state device

Cyclic Voltammetry (CV), Galvanostatic Charge/Discharge (GCD), and Electrochemical Impedance Spectroscopy (EIS) were performed using an Autolab potentiostat, at room temperature. CV was recorded at various potential scan rates, between 100 and $10,000 \, mV \cdot s^{-1}$ in the 0–1 V range. GCD was done at different current densities in the range $0.026–0.52 \, mA \cdot cm^{-2}$. EIS spectra were recorded at a potential of 0.3 V in the frequency range of 10 mHz–50 kHz with an amplitude of 10 mV.

Batteries & Supercaps

Research Article
doi.org/10.1002/batt.202300430

Chemistry Europe
European Chemical
Societies Publishing

Supporting Information

Supporting information is available online. 1. rGO-polydopamine composite preparation and characterizations (Figure S1 and S2, Table S1 and S2); 2. EQCM characterization of rGO (Figure S3); 3. *Ac*-electrogravimetry (Figure S4–S6, Table S3); 4. EIS characterization of rGO and rGO-PDA (Figure S7, Table S4); 5. Microsupercapacitor characterization (Figure S8 and S9); 6. References [48,49].

Conflict of Interests

The authors declare no conflict of interest.

Data Availability Statement

The data that support the findings of this study are available from the corresponding author upon reasonable request.

[1] A. González, E. Goikolea, J. A. Barrena, R. Mysyk, *Renewable Sustainable Energy Rev.* **2016**, *58*, 1189–1206.
[2] D. Chen, Z. Lou, K. Jiang, G. Shen, *Adv. Funct. Mater.* **2018**, *28*, 1805596.
[3] C. García Núñez, L. Manjakkal, R. Dahiya, *npj Flexible Electron.* **2019**, *3*, 1.
[4] T. B. Naveen, D. Durgalakshmi, A. K. Kunhiraman, S. Balakumar, R. Ajay Rakkesh, *J. Mater. Res.* **2021**, *36*, 4102–4119.
[5] X. Chen, Z. Hou, G. Li, W. Yu, Y. Xue, G. Niu, M. Xin, L. Yang, C. Meng, S. Guo, *Nano Energy* **2022**, *101*, 107606.
[6] J. Wang, F. Li, F. Zhu, O. G. Schmidt, *Small Methods* **2019**, *3*, 1800367.
[7] N. Liu, Y. Gao, *Small* **2017**, *13*, 1701989.
[8] S. Zhu, Z. Xu, H. Tao, D. Yang, X. Tang, Y. Wang, *Energy Adv.* **2023**, *2*, 765–783.
[9] C. Zhao, Y. Liu, S. Beirne, J. Razal, J. Chen, *Adv. Mater. Technol.* **2018**, *3*, 1800028.
[10] F. Bu, W. Zhou, Y. Xu, Y. Du, C. Guan, W. Huang, *npj Flexible Electron.* **2020**, *4*, 31.
[11] Z.-S. Wu, X. Feng, H.-M. Cheng, *Natl. Sci. Rev.* **2013**, *1*, 277–292.
[12] J. Liang, A. K. Mondal, D.-W. Wang, F. Iacopi, *Adv. Mater. Technol.* **2019**, *4*, 1800200.
[13] B. Kirubasankar, B. Balan, C. Yan, S. Angaiah, *Energy Technol.* **2021**, *9*, 2000844.
[14] K. S. Novoselov, A. K. Geim, S. V. Morozov, D. Jiang, Y. Zhang, S. V. Dubonos, l. V. Grigorieva, A. A. Firsov, *Science* **2004**, *306*, 666–669.
[15] P. Sutter, *Nat. Mater.* **2009**, *8*, 171–172.
[16] S. Abdolhosseinzadeh, H. Asgharzadeh, H. Seop Kim, *Sci. Rep.* **2015**, *5*, 10160.
[17] F. Banhart, J. Kotakoski, A. V. Krasheninnikov, *ACS Nano* **2011**, *5*, 26–41.

[18] H.-H. Huang, K. K. H. De Silva, G. R. A. Kumara, M. Yoshimura, *Sci. Rep.* **2018**, *8*, 6849.
[19] N. Díez, A. Śliwak, S. Gryglewicz, B. Grzyb, G. Gryglewicz, *RSC Adv.* **2015**, *5*, 81831–81837.
[20] F. Luo, K. Wu, J. Shi, X. Du, X. Li, L. Yang, M. Lu, *J. Mater. Chem. A* **2017**, *5*, 18542–18550.
[21] S. Dong, Z. Xie, Y. Fang, K. Zhu, Y. Gao, G. Wang, J. Yan, K. Cheng, K. Ye, D. Cao, *ChemistrySelect* **2019**, *4*, 2711–2715.
[22] J. Tian, Y. Xue, M. Wang, Y. Pei, H. Zhang, J. Wang, *Electrochim. Acta* **2019**, *296*, 49–58.
[23] J. Li, Y. J. Zou, L. Jin, F. Xu, L. X. Sun, C. L. Xiang, *J. Energy Storage* **2022**, *50*, 104639.
[24] C. Huang, Q. L. Tang, Q. S. Feng, Y. H. Li, Y. L. Xu, Y. Zhang, A. Hu, S. Y. Zhang, W. N. Deng, X. H. Chen, *J. Mater. Chem. A* **2020**, *8*, 9661–9669.
[25] Y. Shao, J. Wang, M. Engelhard, C. Wang, Y. Lin, *J. Mater. Chem.* **2010**, *20*, 743–748.
[26] B. Lesiak, G. Trykowski, J. Tóth, S. Biniak, L. Kövér, N. Rangam, A. Małolepszy, L. Stobiński, *Materials* **2021**, *14*, 5728.
[27] N. Nazi, V. Humblot, C. Debiemme-Chouvy, *Langmuir* **2020**, *36*, 11005–11014.
[28] F. Escobar-Teran, H. Perrot, O. Sel, *Materials* **2022**, *15*, 1867.
[29] H. Goubaa, F. Escobar-Teran, I. Ressam, W. Gao, A. El Kadib, I. T. Lucas, M. Raihane, M. Lahcini, H. Perrot, O. Sel, *J. Phys. Chem. C* **2017**, *121*, 9370–9380.
[30] W. Gao, C. Debiemme-Chouvy, M. Lahcini, H. Perrot, O. Sel, *Anal. Chem.* **2019**, *91*, 2885–2893.
[31] A. Bouzina, H. Perrot, C. Debiemme-Chouvy, O. Sel, *ACS Appl. Energ. Mater.* **2022**, *5*, 14934–14944.
[32] E. M. Halim, R. Demir-Cakan, H. Perrot, M. El Rhazi, O. Sel, *J. Chem. Phys.* **2022**, *156*, 124703.
[33] Y. Zhu, S. Murali, M. D. Stoller, K. J. Ganesh, W. Cai, P. J. Ferreira, A. Pirkle, R. M. Wallace, K. A. Cychosz, M. Thommes, D. Su, E. A. Stach, R. S. Ruoff, *Science* **2011**, *332*, 1537–1541.
[34] A. Bouzina, H. Perrot, O. Sel, C. Debiemme-Chouvy, *ACS Appl. Nano Mater.* **2021**, *4*, 4964–4973.
[35] H. Banda, B. Daffos, S. Périé, Y. Chenavier, L. Dubois, D. Aradilla, S. Pouget, P. Simon, O. Crosnier, P.-L. Taberna, F. Duclairoir, *Chem. Mater.* **2018**, *30*, 3040–3047.
[36] Z. Liu, H. Zhang, M. Eredia, H. Qiu, W. Baaziz, O. Ersen, A. Ciesielski, M. Bonn, H. I. Wang, P. Samorì, *ACS Nano* **2019**, *13*, 9431–9441.
[37] P. Bandyopadhyay, T. Kuila, J. Balamurugan, T. T. Nguyen, N. H. Kim, J. H. Lee, *Chem. Eng. J.* **2017**, *308*, 1174–1184.
[38] Z. Yang, F. Zhou, H.-t. Zhang, J.-q. Qin, Z.-S. Wu, *New. Carbon. Mater.* **2022**, *37*, 936–943.
[39] S. Sollami Delekta, K. H. Adolfsson, N. Benyahia Erdal, M. Hakkarainen, M. Östling, J. Li, *Nanoscale* **2019**, *11*, 10172–10177.
[40] Y. Wang, Y. Zhang, G. Wang, X. Shi, Y. Qiao, J. Liu, H. Liu, A. Ganesh, L. Li, *Adv. Funct. Mater.* **2020**, *30*, 1907284.
[41] J. Ma, S. Zheng, Y. Cao, Y. Zhu, P. Das, H. Wang, Y. Liu, J. Wang, L. Chi, S. Liu, Z.-S. Wu, *Adv. Energy Mater.* **2021**, *11*, 2100746.
[42] A. Ferris, S. Garbarino, D. Guay, D. Pech, *Adv. Mater.* **2015**, *27*, 6625–6629.
[43] R. Agrawal, C. Wang, *Micromachines* **2018**, *9*, 399.
[44] Y. Wang, Y.-Z. Zhang, Y.-Q. Gao, G. Sheng, J. E. ten Elshof, *Nano Energy* **2020**, *68*, 104306.
[45] G. Sauerbrey, *Z. Phys.* **1959**, *155*, 206–222.
[46] K. Bizet, C. Gabrielli, H. Perrot, *Appl. Biochem. Biotechnol.* **2000**, *89*, 139–149.
[47] W. Gao, N. Krins, C. Laberty-Robert, H. Perrot, O. Sel, *J. Phys. Chem. C* **2021**, *125*, 3859–3867.
[48] C. Gabrielli, J. J. Garcia-Jareno, M. Keddam, H. Perrot, F. Vicente, *J. Phys. Chem. B* **2002**, *106*, 3182–3191.
[49] C. Gabrielli, J. J. Garcia-Jareno, M. Keddam, H. Perrot, F. Vicente, *J. Phys. Chem. B* **2002**, *106*, 3192–3201.